Research Article | Vol. 34, No. 13 / 29 Jun 2026 / Optics Express 24703

Optics EXPRESS

# Enhancing resolution of stimulated Raman scattering microscopy

JUN LIU,[1] YAN LIU,[1] AND XIAOLONG SU[1,2,*]

[1] State Key Laboratory of Quantum Optics Technologies and Devices, Institute of Opto-Electronics, Shanxi University, Taiyuan 030006, China
[2] Collaborative Innovation Center of Extreme Optics, Shanxi University, Taiyuan, Shanxi 030006, China
[*] suxl@sxu.edu.cn

**Abstract:** As a powerful tool of biological imaging, stimulated Raman scattering (SRS) microscopy enables rapid, label-free imaging with high molecular specificity. In the application of SRS microscopy, it is essential to break the optical diffraction limit and enhance the resolution. Here, we demonstrate an effective method that combines antiphase demodulation with a deconvolution algorithm to achieve super-resolution SRS imaging. By introducing a donut-shaped pump beam with antiphase modulation in SRS microscopy, the signal around the focal center is effectively suppressed, enabling subdiffraction-limited imaging. Followed by a deconvolution algorithm, we obtain a 3.5-fold improvement in spatial resolution using human hair as a test specimen. The result offers a practical method for super-resolution SRS microscopy without significant sample damage, broadening applications in super-resolution, label-free biological imaging.

© 2026 Optica Publishing Group under the terms of the Optica Open Access Publishing Agreement

## 1. Introduction

As a powerful label-free imaging technique, stimulated Raman scattering (SRS) microscopy has broad applications in biomedical imaging [1–6], medicine research [7–9], and materials science [10–13]. Compared to conventional spontaneous Raman scattering microscopy, SRS microscopy offers orders-of-magnitude improvement in signal strength and imaging speed, making it particularly suitable for real-time imaging of living systems [14–17]. Moreover, in contrast to coherent anti-Stokes Raman scattering, SRS is free from non-resonant background noise and exhibits a linear dependence of signal intensity on sample concentration, enabling more accurate quantitative analysis [18]. From the above comparison, it can be seen that SRS microscopy has the advantage of label-free, high-speed, and high-sensitivity imaging, which has drawn increasing attention.

Driven by the growing demands of numerous imaging applications, advanced techniques have been explored to improve the performance of SRS microscopy [4,19,20]. By employing pulse-shaped femtosecond lasers or multichannel array detectors, high-speed multispectral imaging can be achieved. For example, spectral focusing methods [21–24] and parallel SRS imaging [25,26] have been developed to access a broader range of spectral information. In addition, quantum light sources are employed in place of conventional coherent illumination to enhance imaging signal-to-noise ratio and sensitivity [27–32]. Besides the improvement of spectral information and sensitivity in SRS microscopy, it is also essential to enhance the spatial resolution of SRS microscopy, which is a key parameter of imaging and is limited by the optical diffraction limit.

As a super-resolution imaging technique, stimulated emission depletion (STED) employs a donut-shaped depletion beam to reduce the effective point spread function (PSF) of the imaging system, which has been applied in fluorescence imaging system to improve resolution [33,34]. Inspired by this principle, a STED-like approach is applied in SRS microscopy to enhance the resolution [35]. However, this method requires a high depletion beam power for significant

#605299 https://doi.org/10.1364/OE.605299
Journal © 2026 Received 14 May 2026; revised 16 Jun 2026; accepted 16 Jun 2026; published 24 Jun 2026

Optics EXPRESS

resolution enhancement, which may cause damage to the sample and thus limits its applicability to biological imaging. Recently, it has been shown that the use of a donut-shaped beam with an antiphase modulation enables enhancement of resolution in direct optical inspection of integrated circuits [36]. This approach does not require high optical power, whereas related studies applying this method to SRS imaging remain limited. In addition to the above methods, deconvolution algorithms can also improve resolution in an imaging system, which offers a computational approach to mitigate the blurring introduced by diffraction and optical aberrations of the system [37–39]. By applying PSF-based deconvolution algorithms, such as Richardson-Lucy iteration or regularized inverse filtering, it is possible to suppress artifacts and improve both spatial resolution and image contrast [40]. However, it is unclear how much the resolution can be improved by combining the antiphase demodulation scheme with deconvolution algorithms in SRS microscopy.

Here, we combines antiphase demodulation with a deconvolution algorithm to achieve super-resolution SRS microscopy. By introducing a donut-shaped pump beam with antiphase modulation, the signal around the focal center is effectively suppressed, enabling subdiffraction-limited imaging. Then, we apply a deconvolution algorithm to the acquired image, which further enhances the spatial resolution. The presented method results in a 3.5-fold improvement in resolution beyond the diffraction limit for label-free SRS microscopy. Our method can enhance image resolution without excessive optical power on samples, providing a practical route to super-resolution, label-free biological imaging.

## 2. Antiphase demodulation SRS microscopy

Figure 1(a) illustrates the setup of our antiphase demodulation SRS microscope. The laser source (APE, picoEmerald S) delivers two synchronized picosecond-pulsed beams: a Stokes beam ($\omega_s$) fixed at 1031 nm and a pump beam ($\omega_p$) tunable from 700 to 990 nm. Both beams have a pulse duration of 2 ps and a repetition rate of 80 MHz. When the frequency difference $\Delta\omega = \omega_p - \omega_s$ matches a specific vibrational mode of the sample ($\Omega_{vib}$), energy is coherently transferred from the pump beam to the Stokes beam, leading to a portion intensity consumption in the pump (stimulated Raman loss) and a corresponding intensity increase in the Stokes beam (stimulated Raman gain). This intensity changes for stimulated Raman loss $\Delta I_{\mathrm{SRL}}$ and stimulated Raman gain $\Delta I_{\mathrm{SRG}}$ depend on the molecular concentration $N$, the pump intensity $I_p$ and the Stokes intensity $I_s$, which are given by

$$\Delta I_{\mathrm{SRL,SRG}} \propto N \cdot \sigma_R \cdot I_p \cdot I_s, \tag{1}$$

where $\sigma_R$ is the Raman cross-section of the test sample [6,18].

In our SRS microscopy system, high-speed scanning of the combined beams is achieved using a pair of galvanometric mirrors, allowing rapid image acquisition. To maximize optical throughput, a custom scan lens and tube lens are employed, achieving optical transmission efficiency above 90% for the input beams. The collinear pumps and Stokes beams are then focused into the sample by a water-immersion objective (HC PL IRAPO 40x/1.10 W CORR, Leica) and subsequently directed to a high-NA condenser (U-AAC, Olympus). Following the condenser, residual pump light is rejected by optical filters (FF01-1055/70-25, Semrock), ensuring that only the output Stokes beam reaches the detector. To extract the SRS signal from the strong background, the pump beam is amplitude-modulated at 20 MHz using an electro-optic modulator. After the SRS interaction, the modulation is transferred from pump beam to the Stokes beam. The resulting signal is then demodulated by a lock-in amplifier using a reference signal at the same frequency and subsequently recorded for image reconstruction. This modulation-demodulation method avoids 1/f noise at low frequencies, allowing for detection with high sensitivity.

In the antiphase demodulation approach, we introduce a donut-shaped pump beam with antiphase modulation [41]. We divided the initial Gaussian-profile pump beam into two parts, where the pump-1 beam is also Gaussian-profile and the pump-2 beam is shaped into a vortex

Optics EXPRESS

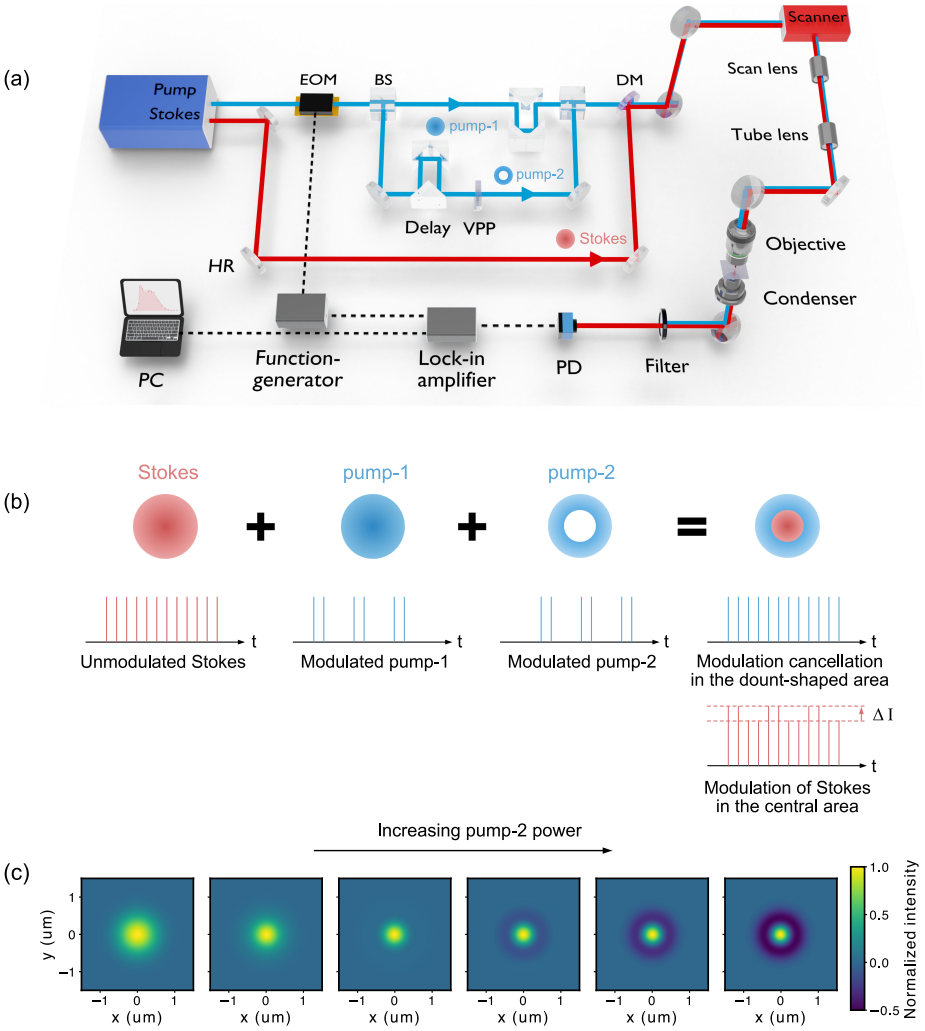


**Fig. 1.** Schematic of antiphase-demodulated SRS microscopy. (a) The experimental setup of antiphase-demodulated SRS microscopy. An antiphase-modulated donut-shaped beam is used to enhance the resolution of the image. EOM, electro-optical modulator; PBS, polarization beam splitter; DM, dichroic mirror; VPP, vortex phase plate; PD, photodiode. (b) The principle of antiphase demodulation SRS microscopy. After amplitude modulation, the Stokes beam, the pump-1 beam, and the donut-shaped pump-2 beam are combined and focused onto the sample. Due to the antiphase demodulation in the donut region, the modulation signal is transferred only at the very center of the Stokes beam. (c) The total PSF of antiphase-demodulated SRS microscopy. As the pump-2 power increases, the PSF spot becomes progressively smaller and eventually exhibits negative values in the peripheral regions.

Optics EXPRESS

beam by a $2\pi$ vortex phase plate, as shown in Fig. 1(a). The pump-1 beam passes through a delay line to synchronize its arrival time with the Stokes pulses at the sample, ensuring efficient SRS interaction. The pump-2 travels through another delay line to introduce a half-modulation-period relative to pump-1. These three beams are then combined using a dichroic mirror and directed into a microscope for the subsequent SRS process. With the antiphase configuration, the donut-shaped pump-2 cancels out the 20 MHz intensity modulation in the annular region, while the modulation at the center of the pump-1 remains unchanged, as shown in Fig. 1(b). Consequently, after the SRS process, the modulation on the pump-1 is transferred to the output Stokes beam at the very center region, resulting in a spatially confined signal and thereby enhancing the resolution of imaging. Figure 1(c) shows the simulated total PSF of the system. As the pump-2 power increases, the PSF spot becomes progressively smaller, indicating an enhancement in the system resolution. With a further increase in pump-2 power, the peripheral regions of the total PSF begin to exhibit negative values, leading to increased loss of the SRS signal.

We use n-dodecane (D807186, Macklin) as a test sample to verify the performance of the SRS microscopy system. A small drop of the liquid is placed on a glass slide and covered with a coverslip to form a thin sample layer. The Stokes beam and pump-1 beam are set to 12 mW at the sample with identical polarization, while the pump-2 beam is blocked. As shown in Fig. 2(a), by tuning the wavelength of the pump beam, the Raman spectrum of n-dodecane is recorded, showing excellent agreement with the conventional spontaneous Raman spectrum [42]. This result indicates that the SRS system can directly leverage existing Raman databases for molecular identification. To further characterize the signal response, the Stokes beam power is varied from 0 mW to 12 mW while the pump power is fixed at 12 mW. This power level is chosen to ensure a strong SRS signal, enabling a clear characterization of its dependence on the excitation powers. As shown in Fig. 2(b), the detected SRS signal increases linearly with the Stokes power, consistent with the theoretical expectation shown in Eq. (1). This linear dependence validates the quantitative capability of the system for molecular concentration analysis.

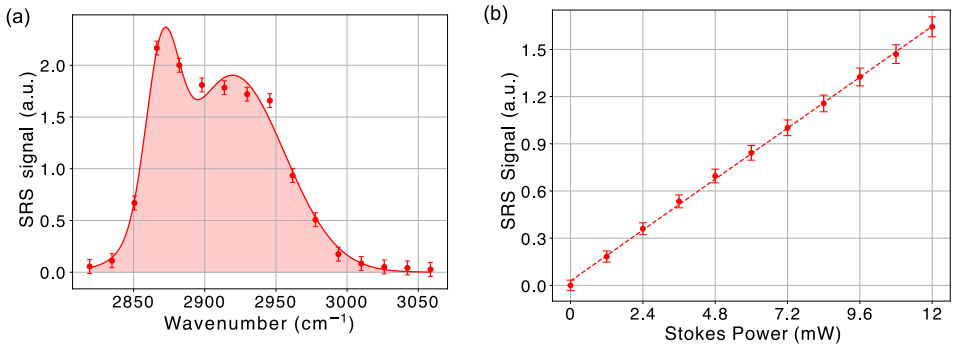


**Fig. 2.** The SRS intensity measurement results of an n-dodecane sample using SRS microscopy. (a) SRS spectrum of n-dodecane. Both the pump-1 and Stokes beam powers are set to 12 mW, and the wavelength of the pump-1 beam is scanned from 784 nm to 799 nm. (b) SRS signal intensity as a function of Stokes power, with the pump-1 power fixed at 12 mW.

After calibrating the microscope with n-dodecane, we evaluate the spatial resolution of SRS microscopy using human hair as a test specimen. The human hair is obtained from a local barber shop (Shanxi, China). Although a hair has an overall diameter of tens of micrometers, its fine internal fibrillar architecture provides submicrometer features and is suitable for resolution characterization. We place a clean human hair on a glass slide and cover it with a cover slip. The SRS images of human hair are acquired using a 6 mW Stokes beam at 1031 nm and a 3 mW pump-1 beam at 792 nm, corresponding to a Raman shift of 2894 $cm^{-1}$. By varying the power of

Optics EXPRESS

the donut-shaped pump-2 beam from 0 mW to 3 mW, an enhancement in spatial resolution is observed, as shown in Figs. 3(a)–3(f), where the insets display a zoom-in view of the selected region.

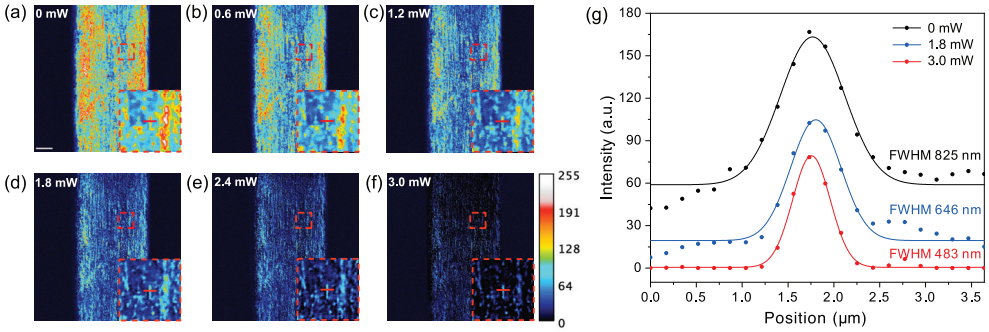


**Fig. 3.** Super-resolution imaging of human hair with antiphase demodulation. (a)-(f) Antiphase demodulation SRS imaging of human hair with donut-shaped pump-2 beam powers varies from 0 mW to 3 mW. Insets show the zoom-in view in the same selected region. The image size is 1024 × 1024 pixels over a field of view of 177 ×177 $\mu$m$^2$ and the pixel dwell time is 2 $\mu$s/pixel. The colorbar indicates the SRS signal intensity in arbitrary units. Scale bar, 20 $\mu$m. (g) Intensity profiles extracted from the selected lines in (a), (d), and (f). The black, blue, and red curves correspond to a donut-shaped beam power of 0 mW, 1.8 mW, and 3 mW, respectively.

To quantitatively evaluate the resolution improvement, Gaussian fitting is performed on the marked lines in Figs. 3(a), 3(d), and 3(f) at the same position. Here, the full width at half maximum (FWHM) of fitted curves is used to represent the resolution of images. As shown in Fig. 3(g), with increasing donut-shaped beam power, the spatial resolution improved from 825 nm at 0 mW to 483 nm at 3 mW, corresponding to a 1.7-fold enhancement. These results demonstrate that the antiphase demodulation effectively suppresses donut area signals while preserving the central focus, thereby enabling sub-diffraction-limited resolution. Remarkably, this enhancement required only 3 mW of donut-shaped beam power, equal to the Gaussian-shaped pump-1 power employed in our setup. In this way, the overall optical load remains within typical SRS operating ranges, relaxing the risk of photodamage to the tested sample.

In our experiments, when the donut-shaped pump-2 power exceeds 3 mW, the SRS signal is reduced by half compared with the case where pump-2 is blocked. This occurs because an excessively high power of the antiphase-modulated donut-shaped beam partially cancels the SRS signal, corresponding to the negative values appearing in the peripheral regions of the total PSF. Therefore, to obtain super-resolution images with a sufficient signal intensity, the power of the donut-shaped beam must be carefully controlled. In addition, for deep-tissue biological imaging, tissue scattering will rapidly degrade the phase integrity of the donut-shaped vortex beam, thereby reducing the achievable resolution enhancement. To mitigate these effects, adaptive optics and wavefront correction strategies are expected to extend the imaging depth in scattering biological tissues [34,43].

## 3. Resolution enhancement with deconvolution

To further enhance the resolution of SRS microscopy, we apply a deconvolution algorithm to the image obtained with an antiphase demodulation scheme. Deconvolution relies on a forward model in which the recorded image $y$ is described as the convolution of the true object $x$ with the

Optics EXPRESS

system PSF $h$,

$$y = x * h + n, \tag{2}$$

where $h$ characterizes the system response to a point source and $n$ denotes photon and detector noise. With an appropriate PSF and deconvolution algorithms, this approach can reduce artifacts and recover more accurate structural information from the recorded image. The PSF of the system can be obtained either experimentally by measuring sub-diffraction beads or theoretically computed from system parameters, such as wavelength, numerical aperture, and refractive index.

Since deconvolution does not depend on a specific imaging method and requires no extra setup, it can be directly applied to SRS microscopy. We deconvolve the images in Figs. 3(a) and 3(f) using the Richardson–Lucy iterative algorithm with a theoretically generated PSF [40,44,45]. The resulting images are presented in Figs. 4(a) and 4(b). Quantitative analysis based on Gaussian fitting at the same position reveals that the resolutions in Figs. 3(a) and 3(f) improve from 825 nm to 551 nm and from 483 nm to 239 nm, respectively, as indicated by the black and red dashed curves in Fig. 4(c). Furthermore, Figs. 3(g) and 4(c) show that antiphase demodulation improves the resolution from 825 nm to 483 nm, and the subsequent deconvolution further improves it to 239 nm. Therefore, by combining the antiphase demodulation and deconvolution approaches, a 3.5-fold enhancement for the resolution of the image is obtained.

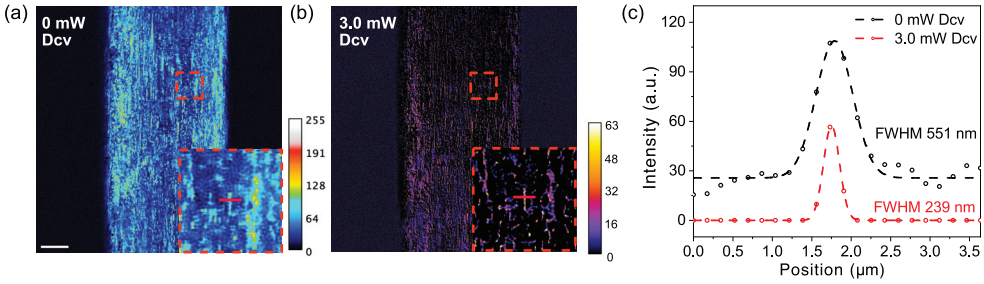


**Fig. 4.** Super-resolution SRS imaging combining antiphase demodulation and deconvolution approaches. (a) The result of the deconvolution of the image in Fig. 3(a). This image shows the impact of the deconvolution method in enhancing the spatial resolution. (b) The result of the deconvolution of the image in Fig. 3(f). This image illustrates the improvement in spatial resolution achieved by combining antiphase demodulation with deconvolution. Insets show magnified views of the selected regions. The colorbar indicates the SRS signal intensity in arbitrary units. Scale bar, 20 $\mu$m. (c) Intensity profiles extracted from the selected lines in Figs 4(a) and 4(b). The black and red dashed curves correspond to the selected lines in Figs. 4(a) and 4(b), respectively.

## 4. Discussion and conclusion

In addition to the resolution enhancement shown in Fig. 4(b), we also notice that the signal intensity is reduced when combining antiphase demodulation and deconvolution schemes. On the one hand, increasing the donut-beam power results in stronger suppression of the SRS signal by the antiphase demodulation scheme, as shown in Fig. 3. On the other hand, the deconvolution process selectively amplifies high-frequency components while attenuating low-frequency ones, resulting in an overall reduction in the apparent signal amplitude. Nevertheless, the combined approach remains meaningful, as the signal loss can be mitigated by longer integration times or frame averaging, whereas the resolution cannot. In our experiment, it takes 2 seconds to acquire a $1024 \times 1024$ pixel image when the combined super-resolution approach is applied. To maintain an acceptable signal-to-noise ratio (SNR) at this enhanced resolution, the acquisition times need to be extended to around 20 seconds.

Optics EXPRESS

To further improve the resolution of the image, a larger numerical aperture of the objective and a shorter wavelength of the input beams can be applied. In our system, the input beam underfilled the back aperture of the objective, making an effective numerical aperture of 0.45 and a corresponding diffraction-limited resolution of 850 nm. By using shorter excitation wavelengths and a larger effective numerical aperture, our scheme could in principle improve the resolution to 60 nm for biological imaging. Furthermore, the use of experimentally measured PSF may improve the quality of image reconstruction, leading to more accurate results. Moreover, combining the above approaches with quantum light sources allows simultaneous improvement of spatial resolution and SNR.

In summary, we demonstrated a method to enhance the spatial resolution of SRS microscopy by combining antiphase demodulation with a deconvolution algorithm. By varying the vortex beam power, we observed a clear trend of resolution improvement with increasing power, realizing a 1.7-fold enhancement of resolution. Furthermore, by employing the deconvolution algorithm on the obtained image, the resolution of the image reaches 239 nm, a 3.5-fold improvement over the diffraction-limited resolution. These results highlight the potential of antiphase demodulation and deconvolution approaches in pushing the spatial resolution of SRS imaging beyond conventional limits, offering a powerful tool for biological imaging.

**Funding.** National Key Scientific Instrument and Equipment Development Projects of China (2022YFF0706002); National Natural Science Foundation of China (U25A20525); Shanxi "1331 Project" Key Subjects Construction.

**Acknowledgment.** The authors would like to thank Minbiao Ji, Yingjie He, and Kuan Luo for their helpful discussions on sample preparation related to this work.

**Disclosures.** The authors declare no conflict of interest.

**Data availability.** Data underlying the results presented in this paper are not publicly available at this time but may be obtained from the authors upon reasonable request.

## References

1. C. W. Freudiger, W. Min, B. G. Saar, *et al.*, "Label-free biomedical imaging with high sensitivity by stimulated Raman scattering microscopy," Science **322**(5909), 1857–1861 (2008).
2. F.-K. Lu, S. Basu, V. Igras, *et al.*, "Label-free DNA imaging in vivo with stimulated Raman scattering microscopy," P. Natl. Acad. Sci. USA **112**(37), 11624–11629 (2015).
3. D. Fu, W. Yang, and X. S. Xie, "Label-free imaging of neurotransmitter acetylcholine at neuromuscular junctions with stimulated Raman scattering," J. Am. Chem. Soc. **139**(2), 583–586 (2017).
4. Y. Li, B. Shen, G. Zou, *et al.*, "Fast denoising and lossless spectrum extraction in stimulated Raman scattering microscopy," J. Biophotonics **14**(8), e202100080 (2021).
5. L. Shi, A. A. Fung, and A. Zhou, "Advances in stimulated Raman scattering imaging for tissues and animals," Quant. Imaging Med. Surg. **11**(3), 1078–1101 (2021).
6. W. Min, J.-X. Cheng, and Y. Ozeki, "Theory, innovations and applications of stimulated Raman scattering microscopy," Nat. Photon. **19**(8), 803–816 (2025).
7. D. Fu, J. Zhou, W. S. Zhu, *et al.*, "Imaging the intracellular distribution of tyrosine kinase inhibitors in living cells with quantitative hyperspectral stimulated Raman scattering," Nat. Chem. **6**(7), 614–622 (2014).
8. M. Kawaguchi, Y. Yonetani, T. Mizuguchi, *et al.*, "Visualization of modified bisarylbutadiyne-tagged small molecules in live-cell nuclei by stimulated Raman scattering microscopy," Anal. Chem. **96**(17), 6643–6651 (2024).
9. M. Wei, N. Qian, X. Gao, *et al.*, "Single-particle imaging of nanomedicine entering the brain," P. Natl. Acad. Sci. USA **121**(5), e2309811121 (2024).
10. Q. Cheng, Z. L. Lu Wei, N. Ni, *et al.*, "Operando and three-dimensional visualization of anion depletion and lithium growth by stimulated Raman scattering microscopy," Nat. Commun. **9**(1), 2942 (2018).
11. J. Ling, X. Miao, Y. Sun, *et al.*, "Vibrational imaging and quantification of two-dimensional hexagonal boron nitride with stimulated Raman scattering," ACS Nano **13**(12), 14033–14040 (2019).
12. A. Jianpeng, F. Yiqing, W. Simin, *et al.*, "Rapid, 3D chemical profiling of individual atmospheric aerosols with stimulated Raman scattering microscopy," Small Methods **4**(2), 1900600 (2020).
13. Q. Cheng, Y. Miao, J. Wild, *et al.*, "Emerging applications of stimulated Raman scattering microscopy in materials science," Matter **4**(5), 1460–1483 (2021).
14. B. G. Saar, C. W. Freudiger, J. Reichman, *et al.*, "Video-rate molecular imaging in vivo with stimulated Raman scattering," Science **330**(6009), 1368–1370 (2010).
15. Z. Wang, W. Zheng, and Z. Huang, "Lock-in-detection-free line-scan stimulated Raman scattering microscopy for near video-rate Raman imaging," Opt. Lett. **41**(17), 3960–3963 (2016).

Optics EXPRESS

16. T. C. Hollon, B. Pandian, A. R. Adapa, *et al.*, "Near real-time intraoperative brain tumor diagnosis using stimulated Raman histology and deep neural networks," Nat. Med. **26**(1), 52–58 (2020).
17. B. Sarri, V. Chevrier, F. Poizat, *et al.*, "In vivo organoid growth monitoring by stimulated Raman histology," npj Imaging **2**(1), 18 (2024).
18. T. Chen, Z. Yu, X. Zhang, *et al.*, "Coherent Raman scattering microscopy," Sci. Sin. Chim. **42**, 1–16 (2012).
19. M. J. Moester, L. Zada, B. Fokker, *et al.*, "Stimulated Raman scattering microscopy with long wavelengths for improved imaging depth," J. Raman Spectrosc. **50**(9), 1321–1328 (2018).
20. C. Kong, C. Pilger, M. Kunisch, *et al.*, "Hyperspectral coherent Raman scattering (CRS) microscopy based on a rapidly tunable and environmentally stable fiber laser," Laser Photonics Rev. **17**(12), 2300521 (2023).
21. E. R. Andresen, P. Berto, and H. Rigneault, "Stimulated Raman scattering microscopy by spectral focusing and fiber-generated soliton as stokes pulse," Opt. Lett. **36**(13), 2387–2389 (2011).
22. M. S. Alshaykh, C.-S. Liao, O. E. Sandoval, *et al.*, "Hyperspectral imaging with stimulated Raman scattering by chirped femtosecond lasers," J. Phys. Chem. B **117**(16), 4634–4640 (2013).
23. D. Fu, G. Holtom, C. Freudiger, *et al.*, "High-speed stimulated hyperspectral Raman imaging using rapid acousto-optic delay lines," Opt. Lett. **42**(8), 1548–1551 (2017).
24. S. Yan, S. Cui, K. Ke, *et al.*, "Hyperspectral stimulated Raman scattering microscopy unravels aberrant accumulation of saturated fat in human liver cancer," Anal. Chem. **90**(11), 6362–6366 (2018).
25. F.-K. Lu, M. Ji, D. Fu, *et al.*, "Multicolor stimulated Raman scattering (SRS) microscopy," Mol. Phys. **110**(15-16), 1927–1932 (2012).
26. K. Seto, Y. Okuda, E. Tokunaga, *et al.*, "Development of a multiplex stimulated Raman microscope for spectral imaging through multi-channel lock-in detection," Rev. Sci. Instrum. **84**(8), 083705 (2013).
27. J. Liu and X. Su, "Quantum-enhanced microscopic imaging technology [invited]," Chin. Opt. Lett. **22**(6), 060010 (2024).
28. R. B. de Andrade, H. Kerdoncuff, K. Berg-Sørensen, *et al.*, "Quantum-enhanced continuous-wave stimulated Raman scattering spectroscopy," Optica **7**(5), 470–475 (2020).
29. C. A. Casacio, L. S. Madsen, A. Terrasson, *et al.*, "Quantum-enhanced nonlinear microscopy," Nature **594**(7862), 201–206 (2021).
30. A. Terrasson, N. P. Mauranyapin, C. A. Casacio, *et al.*, "Fast biological imaging with quantum-enhanced Raman microscopy," Opt. Express **32**(21), 36193–36206 (2024).
31. Z. Xu, K. Oguchi, Y. Taguchi, *et al.*, "Quantum-enhanced stimulated Raman scattering microscopy in a high-power regime," Opt. Lett. **47**(22), 5829–5832 (2022).
32. Z Xu, K. Oguchi, Y. Taguchi, *et al.*, "Stimulated Raman scattering spectroscopy with quantum-enhanced balanced detection," Opt. Express **30**(11), 18589–18598 (2022).
33. S. W. Hell and J. Wichmann, "Breaking the diffraction resolution limit by stimulated emission: stimulated-emission-depletion fluorescence microscopy," Opt. Lett. **19**(11), 780–782 (1994).
34. G. Vicidomini, P. Bianchini, and A. Diaspro, "STED super-resolved microscopy," Nat. Methods **15**(3), 173–182 (2018).
35. R. Silva, C. T. Graefe, and R. R. Frontiera, "Toward label-free super-resolution microscopy," ACS Photonics **3**(1), 79–86 (2015).
36. G. Yang, C. Yang, Y. Chen, *et al.*, "Direct imaging of integrated circuits in CPU with 60 nm super-resolution optical microscope," Nano Lett. **21**(9), 3887–3893 (2021).
37. H. Jang, Y. Li, A. A. Fung, *et al.*, "Super-resolution SRS microscopy with A-PoD," Nat. Methods **20**(3), 448–458 (2024).
38. C. Qiao, Y. Zeng, Q. Meng, *et al.*, "Zero-shot learning enables instant denoising and super-resolution in optical fluorescence microscopy," Nat. Commun. **15**(1), 4180 (2024).
39. L. Qu, S. Zhao, Y. Huang, *et al.*, "Self-inspired learning for denoising live-cell super-resolution microscopy," Nat. Methods **21**(10), 1895–1908 (2024).
40. W. H. Richardson, "Bayesian-based iterative method of image restoration," J. Opt. Soc. AM. A **62**(1), 55–59 (1972).
41. R. Ma, L. Li, X. Qu, *et al.*, "Identifying the asymmetric superposition of fractional orbital-angular-momentum modes via neural networks with a small dataset," Sci. China Inf. Sci. **68**(10), 209406 (2025).
42. ChemicalBook, "Raman spectrum of dodecane," .
43. M. Booth, D. Andrade, D. Burke, *et al.*, "Aberrations and adaptive optics in super-resolution microscopy," Microscopy **64**(4), 251–261 (2015).
44. L. B. Lucy, "An iterative technique for the rectification of observed distributions," Astron. J. **79**, 745–754 (1974).
45. D. Sage, L. Donati, F. Soulez, *et al.*, "DeconvolutionLab2: an open-source software for deconvolution microscopy," Methods **115**, 28–41 (2017).